

# Improved Directional State Transition Tensors for Accurate Aerocapture Performance Analysis

Grace E. Calkins\* and Jay W. McMahon,<sup>†</sup>  
*University of Colorado Boulder, Boulder, CO 80303*

David C. Woffinden<sup>‡</sup>  
*NASA Johnson Space Center, Houston, TX, 77508*

Aerocapture is a unique challenge for semi-analytical propagation because its nonconservative dynamics lead to force magnitudes that vary substantially across the trajectory. State transition tensors (STTs), higher-order Taylor series expansions of the solution flow, have been widely used as a computationally efficient semi-analytical propagation method for orbital scenarios, but have not previously been applied to aerocapture. However, obtaining the higher-order STTs requires integrating exponentially more equations. Directional state transition tensors (DSTTs) mitigate this cost by projecting the state into a reduced-dimension basis. This work develops novel dynamics analysis techniques to identify effective bases for this reduction, including augmented higher-order Cauchy Green tensors tailored to quantities of interest such as apoapsis radius. Results show that DSTTs constructed along these bases significantly reduce computational cost while maintaining accuracy in apoapsis and energy prediction. In particular, certain of these DSTTs outperform traditional DSTTs in nonlinear perturbation propagation for key state subsets and quantities of interest. These results establish STTs and DSTTs as practical tools for aerocapture performance analysis to enable robust guidance and navigation.

## Nomenclature

$\mathbf{A}$	=	Dynamics partials
$\mathbf{C}^{(p)}$	=	$p^{\text{th}}$ -order Cauchy Green tensor
$\mathbf{D}$	=	Drag acceleration
$D_{[p]}$	=	$p^{\text{th}}$ -order coefficient of the quantity-of-interest Taylor series expansion
$H$	=	Exponential atmosphere scale height
$J_2$	=	Second zonal harmonic
$\mathbf{L}$	=	Lift acceleration

\*Ph.D. Pre-Candidate, Department of Aerospace Engineering Sciences. grace.calkins@colorado.edu

<sup>†</sup>Associate Professor, Department of Aerospace Engineering Sciences.

<sup>‡</sup>Aerospace Engineer, GN&C Autonomous Systems Branch

$\frac{L}{D}$	= Lift-to-drag ratio
$Q^{[p]}$	= $p^{\text{th}}$ -order quantity-of-interest Cauchy Green tensor
$\tilde{Q}^{[p]}$	= $p^{\text{th}}$ -order non-symmetric quantity-of-interest Cauchy Green tensor
$\mathbf{R}_{[p]}$	= $p^{\text{th}}$ -order DSTT rotation matrix
$R_p$	= Planet's radius
$\mathbf{S}$	= Selection matrix
$S^{[p]}$	= $p^{\text{th}}$ -order selective Cauchy Green tensor
$\tilde{S}^{[p]}$	= $p^{\text{th}}$ -order non-symmetric selective Cauchy Green tensor
$V$	= Planet-relative velocity
$a$	= Semi-major axis
$a_{\text{ratio}}$	= Ratio of aerodynamic to gravitational accelerations
$f$	= Nonlinear dynamics function
$g_\phi$	= Latitudinal component of gravity
$g_r$	= Radial component of gravity
$h$	= Altitude
$h_0$	= Exponential atmosphere reference height
$m_{\text{ref}}$	= Reference mass
$p_d$	= Dynamic pressure
$q$	= Quantity of interest function
$r$	= Radial distance from the center of the planet
$r_a$	= Apoapsis radius
$\mathbf{x}$	= Vehicle state vector
$\mathbf{y}$	= Reduced-dimension state vector for DSTTs
$\Phi$	= State transition matrix
$\tilde{\Phi}^{[p]}$	= Non-symmetric Cauchy Green of order $p$
$\Omega$	= Planet's constant angular velocity
$\beta$	= Vehicle ballistic coefficient
$\gamma$	= Flight path angle
$\varepsilon$	= Specific orbital energy
$\zeta$	= Natural log of density
$\eta^{i,\dots}$	= Partial of quantity of interest with respect to the state
$\theta$	= Latitude

$\lambda$	= Eigenvalue
$\mu$	= Planet's gravitational parameter
$\xi$	= Selected states
$\rho$	= Atmospheric density
$\rho^*$	= Nondimensional atmospheric density
$\rho_0$	= Exponential atmosphere reference density
$\sigma$	= Bank angle
$\phi$	= Longitude
$\phi$	= Solution flow
$\phi^{i, \gamma_1 \dots \gamma_{p-1}}, \phi^{[p]}$	= $p^{\text{th}}$ -order state transition tensor
$\psi$	= Heading angle
$\psi_{[p]}^{i, \dots}$	= $p^{\text{th}}$ -order DSTT element

## I. Introduction

**A**ERO CAPTURE is increasingly important for sending high-mass missions to explore outer planets, as evidenced by the Uranus Orbiter Probe mission [1]. Aerocapture is an alternative to propulsive orbit insertion in which the spacecraft flies through the atmosphere of a planet to capture into orbit. An aerocapture trajectory is characterized by inherent nonlinearities and potentially large deviations from the desired state. This paper first seeks to determine if state transition tensors (STTs), a computationally efficient analytical uncertainty propagation method previously applied to orbital scenarios, provide similar benefits when applied to nonconservative aerocapture dynamics. Next, it aims to identify if the complexity of the STTs for aerocapture can be reduced through directional state transition tensors (DSTTs). STTs are essentially a higher-order Taylor series expansion of the trajectory dynamics, and DSTTs are a reduced-dimension representation of the STTs along a dynamically-important direction [2–4]. When constructing a DSTT with a single latent dimension, nonlinear perturbation and moment propagation is simplified to matrix-vector multiplication rather than tensor contraction.

This makes DSTTs advantageous compared to other common uncertainty quantification methods. Although Monte Carlo simulation is a prevalent nonlinear uncertainty quantification method for such scenarios, its high computational cost makes it infeasible for onboard implementation. To incorporate uncertainty in a stochastic guidance algorithm, there is a need for more computationally efficient methods that can still capture large initial error distributions and the inherent nonlinearities of the problem. Other computationally efficient uncertainty quantification methods, such as Linear Covariance Analysis [5, 6], Polynomial Chaos Expansion [7, 8], and the Unscented Transform [9], have been explored for aerocapture uncertainty propagation. However, these methods have a few limitations. Linear Covariance

Analysis cannot adequately capture nonlinear effects of the aerocapture dynamics in covariance propagation because the covariance dynamics are linearized. Polynomial Chaos Expansion suffers from the curse of dimensionality, and thus cannot be used when a greater number of states, such as atmospheric or navigation parameters, need to be dispersed. While the Unscented Transform can estimate mean and covariance up to second-order accuracy of the nonlinear transformation, it is computationally expensive, requiring  $2n + 1$  numerical integrations of the nonlinear dynamics model at each simulation timestep (where  $n$  is the number of states). STTs and DSTTs are beneficial compared to these methods because we can directly compute quantities relevant to uncertainty propagation (such as the nonlinearity metrics for Gaussian mixture model construction and guidance presented in [10, 11]).

DSTTs offer a more efficient representation of nonlinear dynamics than standard STTs, as they require fewer terms. Because of this, fewer equations must be integrated to obtain DSTTs than STTs. However, the greatest challenge in using DSTTs is selecting the dynamically important direction along which to reduce the basis dimension. The original DSTT formulation used the dominant eigenvector of the second-order Cauchy-Green tensor (CGT), the direction of maximum stretching in the linear dynamics, to construct DSTTs for orbital scenarios [4]. However, the authors [12, 13] found in previous work that directionalizing the DSTTs along the second-order CGT dominant eigenvector, as had been done in the original DSTT work on orbital scenarios [4, 14], did not result in accurate propagation for aerocapture.

Recently, Zhou et al. developed a method in which they map a time-varying second-order dominant CGT eigenpair without needing to integrate the STTs [15]. This eliminates the need to compute the second-order CGT stretching directions in advance of constructing the DSTTs. However, this method necessitates identifying the dominant eigenvalues a priori. If the relative eigenvalue magnitudes change throughout the trajectory (which can happen in nonconservative systems), and the proper eigenpairs are not selected, the DSTT could no longer be an accurate approximation of the original STT. Thus, it is prudent to use multiple latent dimensions with this method to ensure that the maximal eigenvalue is always incorporated into the DSTT construction. This means a key benefit of DSTTs, only requiring matrix-vector multiplication rather than tensor contraction when using a single latent dimension, is lost. In addition, the time-varying DSTT method uses the eigenpairs of the second-order CGT to construct DSTTs, meaning only stretching due to the linear dynamics is considered. While this method is beneficial for reducing the number of equations to compute DSTTs onboard, it does not consider higher-order dynamics when constructing DSTTs. In the present work, we construct DSTTs along directions associated with nonlinear deformation a priori, rather than computing a time-varying direction along-the-way. As the STTs are nonlinear mappings of the state, we aim to construct DSTTs considering the higher-order sensitivity.

This work seeks to address key limitations in current DSTT theory to improve their performance for nonlinear dynamics such as aerocapture. In previous work, the authors [12, 13] and Zhou et al. [16], found the direction along which DSTTs are constructed was selected based on an important factor in the application rather than the direction of maximum linear stretching. These studies used a heuristic direction scaled by dynamic pressure for aerocapture

and directions informed by uncertainty for orbit determination to construct DSTTs. In this work, we seek to find dynamically-sensitive directions from the STTs to construct accurate DSTTs. We develop a general method to find a higher-order sensitive directions in the dynamics that can be applied to any nonconservative, nonlinear dynamics for which STTs have been obtained.

Additionally, while prior work on orbital dynamics found that (1) the maximal second-order CGT eigenvector direction is relatively constant throughout the trajectory [4, 14] and (2) the higher-order stretching directions align with the lower-order directions [4], this paper shows that this is not true for aerocapture. It is demonstrated that nonconservative aerodynamic forces are the impetus for the time-varying nature of the unstable direction. To construct improved DSTTs, sensitive directions are selected using tensor eigenpairs of novel augmented higher-order Cauchy Green Tensors (HOCGTs). Tensor eigenpairs are the higher-order analog to the matrix eigenproblem, and have been shown to identify directions of strong nonlinearity [17]. The augmented HOCGTs identify directions of maximum stretching for a selected subset of the state or a quantity-of-interest that is an arbitrary function of the state.

This paper is organized as follows. First, the aerocapture problem is presented in Section II. Then, STTs and DSTTs are introduced in Section III. Third, dynamics analysis techniques using functions of the STTs are presented in Section IV, including decomposed CGTs showing the time-varying direction and augmented HOCGTs. In Section V, results are presented showing STT sufficiency for aerocapture perturbation propagation, DSTT approximation accuracy, and DSTT performance for propagating key quantities of interest. Finally, conclusions are given in Section VI.

## II. The Aerocapture Problem

The vehicle state is  $\mathbf{x} = [r, \theta, \phi, V, \gamma, \psi, \zeta]^T$ , where  $r$  is the radial distance from the center of the planet,  $\theta$  and  $\phi$  are the latitude and longitude,  $V$  is the planet-relative velocity,  $\gamma$  is the flight path angle,  $\psi$  is the heading angle, and  $\zeta = \ln(\rho)$  is the natural log of density. Although density is not commonly used as a state variable, density is used here to include atmosphere variation in state perturbations. The 3DOF equations of motion for the spacecraft inside the atmosphere of a rotating planet are [18, 19]:

$$\dot{r} = V \sin \gamma, \quad (1)$$

$$\dot{\theta} = \frac{V \cos \gamma \sin \psi}{r \cos \phi}, \quad (2)$$

$$\dot{\phi} = \frac{V \cos \gamma \cos \psi}{r}, \quad (3)$$

$$\dot{V} = -D - g_r \sin \gamma - g_\phi \cos \gamma \cos \phi + \Omega^2 r \cos \phi (\sin \gamma \cos \phi - \cos \gamma \sin \phi \cos \psi), \quad (4)$$

$$\begin{aligned} \dot{\gamma} = & \frac{1}{V} \left[ L \cos \sigma + \left( V^2/r - g_r \right) \cos \gamma + g_\phi \sin \gamma \cos \psi + 2\Omega V \cos \phi \sin \psi \right. \\ & \left. + \Omega^2 r \cos \phi (\cos \gamma \cos \phi + \sin \gamma \cos \psi \sin \phi) \right], \end{aligned} \quad (5)$$

$$\dot{\psi} = \frac{1}{V} \left[ \frac{L \sin \sigma}{\cos \gamma} + \frac{V^2}{r} \cos \gamma \sin \psi \tan \phi + g_\phi \frac{\sin \psi}{\cos \gamma} - 2\Omega V (\tan \gamma \cos \psi \cos \phi - \sin \phi) \right] \quad (6)$$

$$+ \frac{\Omega^2 r}{\cos \gamma} \sin \psi \sin \phi \cos \phi \right], \quad \text{and}$$

$$\dot{\zeta} = -\frac{V \sin \gamma}{H}, \quad (7)$$

where  $\sigma$  is the bank angle,  $L$  and  $D$  are the lift and drag accelerations,  $\Omega$  is the planet's constant angular velocity,  $R_p$  is the planet's radius, and  $H$  is the exponential atmosphere scale height. These equations assume a spherical planet and that the planet's angular velocity is constant.

The equations to compute the latitudinal and longitudinal components of the gravity vector ( $g_\theta$  and  $g_\phi$ ) are:

$$g_r = \frac{\mu}{r^2} \left[ 1 + J_2 \left( \frac{R_p}{r} \right)^2 (1.5 - 4.5 \sin^2 \phi) \right] \quad (8)$$

$$g_\phi = \frac{\mu}{r^2} \left[ J_2 \left( \frac{R_p}{r} \right)^2 (3 \sin \phi \cos \phi) \right] \quad (9)$$

where  $\mu$  is the planet's gravitational parameter and  $J_2$  is the second zonal harmonic. Lift and drag accelerations are computed as  $L = \frac{1}{2}\rho V^2 \frac{L}{D} \beta$  and  $D = \frac{1}{2}\rho V^2 \beta$ , where the lift-to-drag ratio  $\frac{L}{D} = 0.25$  and the ballistic coefficient  $\beta = 145 \text{ kg/m}^2$ . These values were selected to be similar to the proposed Uranus Orbiter Probe mission [1, 20].

Some considerations were taken to improve the numeric stability of the equations of motion for aerocapture. Given the high sensitivity of the dynamics to atmospheric density, incorporating density as a state variable helps reduce sensitivity in the partial derivatives used to compute the STTs. To address the significant variation in density along the trajectory (approximately five orders of magnitude), the natural logarithm of density is used as a state variable, effectively reducing variability. This equation of motion was derived assuming an exponential atmosphere model  $\rho = \rho_0 \exp \frac{h_0 - (r - R_p)}{H}$ , where the reference density  $\rho_0 = 6.40 \text{e-3 kg/m}^3$ , the reference height  $h_0 = 0 \text{ km}$ , and the scale height  $H = 54.72 \text{ km}$ . The exponential atmosphere constants were found by performing a fit to data from UranusGRAM with a density perturbation scale of two [21]. Additionally, the nondimensionalization scheme developed by Lu was implemented [22]. The nondimensional ODEs are equivalent to the dimensional ODEs in Eqs. (1-7), except that all dimensional variables are replaced with their nondimensional counterparts. A natural log of density normalization factor  $\zeta_{\text{ref}} = 20$  was also introduced, and the natural log of density is normalized as  $\zeta^* = \zeta / \zeta_{\text{ref}}$ .

The initial state for the results presented in the paper is given in Table 1, where the initial radial position is given as an altitude and  $r_0 = h_0 + R_p$ . These values are chosen to be similar to the Flagship-class Uranus Orbiter Probe mission [20]. Trajectories are simulated for 780 seconds to encompass the atmospheric flight duration.

The dynamic pressure profile,  $p_d = \frac{1}{2}\rho V^2$ , and ratio of gravitational to aerodynamic accelerations,  $a_{\text{ratio}} = \sqrt{(L^2 + D^2)/(g_r^2 + g_\phi^2)}$ , for this trajectory are shown in Fig. 1. High dynamic pressure (and greater aerodynamic

**Table 1 Initial State. Initial velocity and flight path angle are in the inertial frame.**

$h$ [km]	$\theta$ [ $^\circ$ ]	$\phi$ [ $^\circ$ ]	$V$ [km/s]	$\gamma$ [ $^\circ$ ]	$\psi$ [ $^\circ$ ]	$\zeta$ [ $\ln(\text{kg/m}^3)$ ]	$\sigma$ [ $^\circ$ ]
1000	190.05	-9.76	24.93	-10.58	45	-23.32	78

acceleration) corresponds to high nonlinearity in the dynamics, and identifying this region is important for the following discussions.

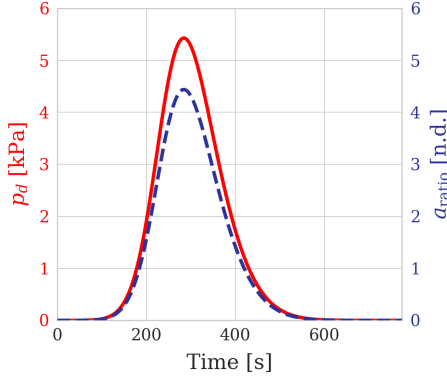


**Fig. 1 Dynamic pressure profile for the nominal trajectory.**

Key quantities of interest for aerocapture are apoapsis radius  $r_a$ ,

$$r_a = a \left( 1 + \sqrt{1 - \frac{V^2 r^2 \cos^2 \gamma}{\mu a}} \right), \quad (10)$$

where  $a$  is the semi-major axis defined as:

$$a = \frac{\mu}{\frac{2\mu}{r} - V^2}, \quad (11)$$

and specific orbital energy  $\varepsilon$ ,

$$\varepsilon = \frac{V^2}{2} - \frac{\mu}{r}. \quad (12)$$

### III. Higher-Order Taylor Series for Perturbation Propagation

As seen in the previous section, the aerocapture problem is highly nonlinear, so linear propagation schemes are not typically sufficient to accurately propagate state perturbations. While small deviations may remain within the linear regime for the initial portion of flight, inherent nonlinearities can rapidly lead to inaccuracies when only using linear propagation. This work employs STTs to nonlinearly and efficiently propagate aerocapture state perturbations. Previous work has shown that accurate reduced-dimension DSTTs can be constructed for orbital scenarios; however, this approach has not been extended to atmospheric flight [4, 15, 16]. Once the STTs are obtained for a particular flight scenario,

they contain rich information about the dynamics, which can be used to construct the reduced-dimension DSTTs that efficiently propagate perturbations. Understanding how to accurately model perturbations is the basis for uncertainty propagation, which will be the focus of future work.

### A. State Transition Tensors

STTs are a higher-order extension of the commonly used state transition matrix (STM). The solution to a dynamic system with state vector  $\mathbf{x} \in \mathbb{R}^n$  can be represented using the solution flow,  $\phi$ , where

$$\mathbf{x}(t) = \phi(t; \mathbf{x}_y, t_y), \quad (13)$$

for given initial condition  $\mathbf{x}_y$  at time  $t_y$  [2, 3]. The STTs are the partial matrices of this solution flow with respect to the state at a previous time  $\mathbf{x}_y$ ,

$$\phi_{(t_z, t_y)}^{i, \gamma_1 \dots \gamma_p} = \frac{\partial^p \phi^i(t_z; \mathbf{x}_y, t_y)}{\partial x_y^{\gamma_1} \dots \partial x_y^{\gamma_p}}. \quad (14)$$

This time indexing will be used throughout the paper for generality to any  $\Delta t = t_z - t_y$ . In addition, index notation is used throughout this paper, where superscripts indicate the components of a tensor and subscripts indicate the time of a vector or the times a matrix or tensor maps between. Repeated superscript indices are summed over, and commas in superscripts separate components that are summed over from those which are not. The number of superscripts indicates the order of the tensor. For example, a second-order tensor is a matrix, a third-order tensor is a three-dimensional tensor, and so on.\* The STTs can be obtained by integrating the variational equations, which can be found in prior work [3]. A perturbation can be propagated through  $m^{\text{th}}$ -order STTs following [3]:

$$\delta x_z^i = \sum_{p=1}^m \frac{1}{p!} \phi_{(t_z, t_y)}^{i, \gamma_1 \gamma_2 \dots \gamma_p} \delta x_y^{\gamma_1} \delta x_y^{\gamma_2} \dots \delta x_y^{\gamma_p} \quad (15)$$

As with the STM, once a set of STTs at points across a time domain  $[t_0, t_f]$  are obtained, they can be manipulated to map over another time domain within the original time domain. Once the STTs are obtained on the interval  $[t_0, t_f]$ , the STT mapping from time  $t_y$  to  $t_z$ , where  $t_y, t_z \in [t_0, t_f]$ , can be computed algebraically [2]. This is especially relevant for spacecraft missions with minimal onboard storage. While it may be useful to use STTs mapping from  $t_k$  to  $t_{k+1}$  for navigation and filtering purposes, guidance may desire to find a higher-order solution from  $t_k$  to  $t_f$ . Uncertainty propagation methods could employ a mapping from  $t_0$  to  $t_k$ . This allows a perturbation to the state to be mapped nonlinearly onboard over any time domain with a single set of STTs computed offline.

---

\*Note that the STM is the first-order STT which is a matrix, and the second-order STT is a third-order tensor. The order of an STT is determined by the number of copies of  $\delta \mathbf{x}$  with which it is contracted.

## B. Directional State Transition Tensors

Higher-order STTs require  $\sum_{i=2}^m n^i$  terms to adequately capture the nonlinear effects, where  $m$  is the STT order and  $n$  is the number of states. As it is computationally expensive to integrate the  $\sum_{i=1}^{m+1} n^i$  variational equations for an  $m^{\text{th}}$ -order STT and can be complex to perform tensor contractions to propagate perturbations (or moments of a distribution for an uncertainty propagation application), constructing a reduced-dimension representation of the STTs is advantageous. Boone and McMahon observed that many of the higher-order STT terms are negligible for orbital equations of motion [4]. The central challenge that follows is to construct a reduced-dimension STT that has a similar effect to the full STT when used for perturbation propagation.

DSTTs are constructed through aligning the STTs with sensitive directions in the dynamics and neglecting the STT terms in the stable directions. Let  $\mathbf{R}_{[p]} \in \mathbb{R}^{l \times n}$ , where  $l \leq n$ , be a linear transformation matrix where  $l$  is the number of sensitive directions and  $p$  is the DSTT order, which is the same as the STT order it is constructed from. The rows of  $\mathbf{R}_{[p]}$  are the orthogonal sensitive directions we seek to align the STTs with. The DSTTs propagate the reduced-dimension perturbation  $\delta\mathbf{y} = \mathbf{R}_{[p]}\delta\mathbf{x}$  through time instead of the full state  $\delta\mathbf{x}$ . The STT derivatives are taken with respect to the state vector  $\mathbf{x} \in \mathbb{R}^n$ , as seen in Eq. (14), whereas the DSTTs can be seen as “rotated” STTs such that their derivatives are taken with respect to another basis,  $\mathbf{y} \in \mathbb{R}^l$ . The second- and third- order DSTTs can be obtained from the STTs by employing the chain rule, using the relations [4],

$$\psi_{[2]}^{i,\gamma_1\gamma_2} = \phi^{i,\kappa_1\kappa_2} R_{[2]}^{\gamma_1,\kappa_1} R_{[2]}^{\gamma_2,\kappa_2}, \quad \text{and} \quad (16)$$

$$\psi_{[3]}^{i,\gamma_1\gamma_2\gamma_3} = \phi^{i,\kappa_1\kappa_2\kappa_3} R_{[3]}^{\gamma_1,\kappa_1} R_{[3]}^{\gamma_2,\kappa_2} R_{[3]}^{\gamma_3,\kappa_3}, \quad (17)$$

where  $\phi^{i,\kappa_1\dots\kappa_p}$  are the elements of the  $p^{\text{th}}$ -order STTs and  $\psi_{[p]}$  is the  $p^{\text{th}}$ -order DSTT. Time indices are omitted for clarity. This expression differs from the original expression presented in [4], as it does not assume that the same  $\mathbf{R}$  matrix is used for each DSTT order. Choosing  $l < n$  reduces the number of terms required to nonlinearly propagate perturbations to the trajectory while significantly lowering storage and computation requirements. For example, a second-order STT has  $n^3$  elements, but a second-order DSTT with  $l = 1$  has only  $n$  terms. Thus, the DSTTs with  $l < n$  are a reduced-dimension, higher-order representation of the solution flow.

In order for DSTTs to be effective, the matrix  $\mathbf{R}_{[p]}$  through which the STTs are transformed to reduce the basis dimension must be a direction which captures the higher-order effects of the STTs, and the dimension of the reduced basis must be sufficient to capture the higher-order effects of the dynamics. In previous studies, the rows of rotation direction matrix  $\mathbf{R}_{[p]}$ , for all orders  $p$ , have been chosen to be the eigenvectors of the largest  $l$  eigenvalues of the second-order CGT [4], where the second-order CGT is defined as:

$$\mathbf{C}_{(t_z,t_y)}^{[2]} = \boldsymbol{\Phi}_{(t_z,t_y)}^{\top} \boldsymbol{\Phi}_{(t_z,t_y)}, \quad (18)$$

where  $\Phi_{(t_z, t_y)}$  is the state transition matrix from  $t_y$  to  $t_z$ . The motivation for using second-order CGT eigenpairs to construct DSTTs is discussed in depth in Section IV. By evaluating the CGT over each regime of interest for propagation, the eigenvectors to construct  $\mathbf{R}_{[p]}$  can be obtained for a given propagation interval.

Similarly to STTs, DSTTs can be used to propagate a perturbation to the state. In order to retain first-order accuracy, the full STM is used and all higher-order STTs are represented as DSTTs in the reduced basis. A deterministic perturbation can be propagated through the  $m^{\text{th}}$ -order DSTTs from  $t_y$  to  $t_z$  as [4]:

$$\delta x_z^i \simeq \phi^{i, \kappa_1} \delta x_y^{\kappa_1} + \sum_{p=2}^m \frac{1}{p!} \psi_{[p]}^{i, \gamma_1 \gamma_2 \dots \gamma_p} \delta y_y^{\gamma_1} \delta y_y^{\gamma_2} \dots \delta y_y^{\gamma_p}. \quad (19)$$

Time subscripts are omitted from the STM and DSTTs for clarity. The  $\delta y$  for order  $p$  is computed using  $\mathbf{R}_{[p]}$ .

For orbital scenarios, DSTTs constructed using the top  $l$  magnitude eigenpairs of the second-order CGT have been sufficient [4, 14–16]. However, some findings in this previous work do not hold true for the aerocapture. Although previous work found little variation between  $\mathbf{R}_{[p]}$ 's for each time domain across an orbit [14], each DSTT propagation interval  $(t_z, t_y)$  has a different  $\mathbf{R}_{[p]}$  in this work because the direction changes greatly throughout the trajectory. While the second-order CGT eigenvectors proved sufficient to construct DSTTs that preserved the effects from the STTs for orbital scenarios [4, 14–16], this method has been found to be inaccurate for aerocapture [12, 13]. In addition, the direction of maximum stretching in the nonlinear dynamics was previously shown to be well-aligned with the direction of linear maximum stretching (the eigenvector of the maximum eigenvalue of the second-order CGT) [4], and this direction was relatively constant throughout the orbit [14]. However, the analysis in the following sections will show that these two findings do not hold true for aerocapture.

## IV. Aerocapture Dynamics Analysis Using Taylor Series

Once STTs have been computed along the full trajectory, they enable a variety of dynamics analysis tools. The following section shows how STTs can be employed to determine the sources of temporal variability of the maximal *linear* stretching direction. We will then use STTs facilitate the identification of directions of maximum *nonlinear* stretching for the entire state, subsets of the state, or nonlinear functions of the state. The information gained from these tools underscore why STTs are beneficial: once the STTs are obtained, a variety of information about the dynamics can be computed and used to construct more accurate reduced-order perturbation propagation methods.

### A. Decomposed Cauchy Green Tensors

Jenson et al. proved that the initial perturbation direction on the unit hypersphere that maximizes the final state perturbation magnitude is the eigenvector corresponding to the maximum eigenvalue of the second-order CGT, computed using Eq. (18) [23]. A perturbation along this direction will yield the largest magnitude change in the final state. While

previous studies have found that this direction is near constant for certain orbital mechanics problems [4, 14], the authors found that this was not the case for aerocapture [12, 13]. To demonstrate the cause of this discrepancy, we separate the aerocapture dynamics into two functions: one for the conservative rotational and gravitational accelerations, and one for the dissipative aerodynamic accelerations. The CGTs of each of these dynamics are evaluated separately to demonstrate the cause of temporal variation in the maximal second-order CGT eigenvector direction.

Given a vector-valued nonlinear dynamics function  $\dot{\mathbf{x}} = f(\mathbf{x})$ ,

$$f(\mathbf{x}) = f_C(\mathbf{x}) + f_D(\mathbf{x}), \quad (20)$$

where  $f_C(\mathbf{x})$  are the conservative dynamics and  $f_D(\mathbf{x})$  are the dissipative dynamics, the first-order Taylor series expansion of  $f$  about the reference trajectory  $\bar{\mathbf{x}}$  is:

$$f(\mathbf{x}) \approx f(\bar{\mathbf{x}}) + \left. \frac{\partial f}{\partial \mathbf{x}} \right|_{\bar{\mathbf{x}}} \delta \mathbf{x} = f(\bar{\mathbf{x}}) + \mathbf{A} \delta \mathbf{x}, \quad (21)$$

where  $\mathbf{A} = \left. \frac{\partial f}{\partial \mathbf{x}} \right|_{\bar{\mathbf{x}}}$ . Evaluating  $f(\mathbf{x})$  with Eq. (20) at the reference state  $\bar{\mathbf{x}}$ ,

$$f(\bar{\mathbf{x}}) = f_C(\bar{\mathbf{x}}) + f_D(\bar{\mathbf{x}}), \quad (22)$$

and taking its first derivative,

$$\left. \frac{\partial f}{\partial \mathbf{x}} \right|_{\bar{\mathbf{x}}} = \left. \frac{\partial f_C}{\partial \mathbf{x}} \right|_{\bar{\mathbf{x}}} + \left. \frac{\partial f_D}{\partial \mathbf{x}} \right|_{\bar{\mathbf{x}}} = \mathbf{A}_C + \mathbf{A}_D, \quad (23)$$

the first-order Taylor series expansion in Eq. (21) becomes:

$$f(\mathbf{x}) \approx f_C(\bar{\mathbf{x}}) + f_D(\bar{\mathbf{x}}) + (\mathbf{A}_C + \mathbf{A}_D) \delta \mathbf{x}, \quad (24)$$

A STM solves the variational equation:

$$\dot{\Phi} = \mathbf{A} \Phi. \quad (25)$$

STMs for the decomposed dynamics can be found using the separated variational equations:

$$\dot{\Phi}_C = \mathbf{A}_C \Phi_C, \quad \text{and} \quad \dot{\Phi}_D = \mathbf{A}_D \Phi_D. \quad (26)$$

The directions that maximize final perturbation magnitude under the  $f_i$  linearized dynamics function can be shown to be the direction corresponding to the maximal eigenvector of the CGT computed using  $\Phi_i$  [17, 23].

The CGTs using the decomposed STM were evaluated along the reference trajectory on the interval  $(t_{k+1}, t_k)$ ,

and the eigenvector corresponding to the maximum eigenvalue is shown in Fig. 2. The overall direction is clearly time-varying, and the large magnitude changes in the velocity and density coordinates result from the aerodynamic portion of the equations of motion, while the conservative equations of motion have a relatively constant direction throughout the entire trajectory. As expected, density plays no role in the conservative dynamics. The region of high variation in eigendirection corresponds to the ratio of aerodynamic to gravitational accelerations exceeding one in Fig. 1, corroborating that the aerodynamic portion of the equations of motion causes the most nonlinearity in the dynamics. This finding demonstrates why a time-varying direction is required to construct DSTTs for aerocapture, even though this is not essential for orbital scenarios.

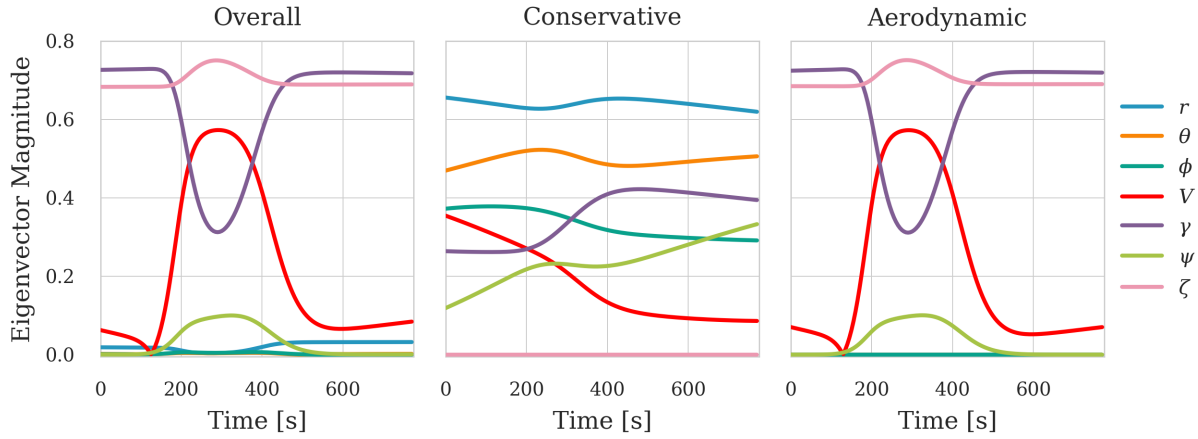


**Fig. 2 Eigenvectors for the maximum eigenvalue for each decomposed dynamics second-order CGT from  $(t_{k+1}, t_k)$ .**

Fig. 2 also shows that the maximum eigenvector overall is more similar to the aerodynamic eigenvector, indicating that the aerodynamic accelerations dominate the equations of motion. As the magnitude of a CGT eigenvalue reflects the local stretching or contraction rate, eigenvectors with larger eigenvalues denote directions along which the perturbation are most amplified in the dynamics. Fig. 3 shows the angle between the eigenvector corresponding to each mode of the overall CGT and the maximal eigenvectors of the decomposed aerodynamic and conservative CGTs. The maximum value of the eigenvalue of the overall dynamics corresponding to each eigenvector is provided in the legend. The dominant CGT eigenvector of the aerodynamic CGT clearly corresponds to the dominant mode of the overall CGT, as the angle is near zero for all times between the dominant aerodynamic eigenvector and dominant overall eigenvector (the eigenvector of maximum eigenvalue  $\lambda_1$  in the overall dynamics). The dominant mode of the conservative CGT best match the second mode of the overall dynamics, corresponding to eigenvalue  $\lambda_2$ , which has a 22% difference in maximum magnitude from  $\lambda_1$ .

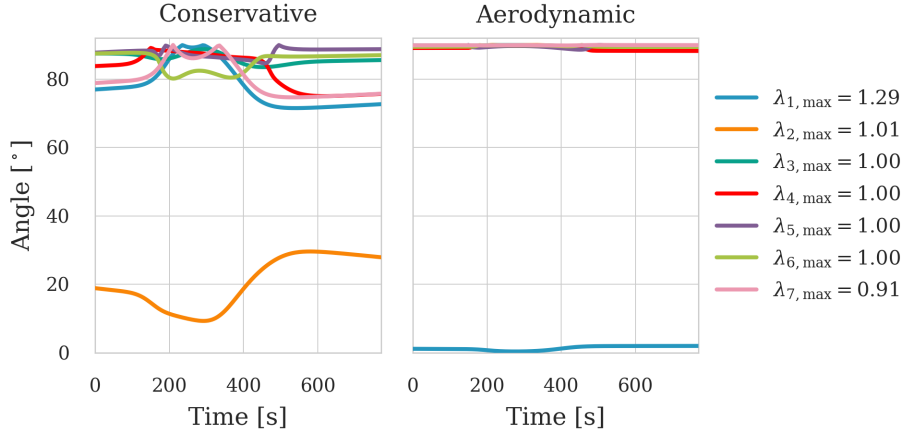


**Fig. 3** Angle between dominant decomposed dynamics CGT eigenvector and all overall CGT eigenvectors.

### B. Tensor Eigenpairs of Higher-Order Cauchy Green Tensors

Aerocapture is a highly nonlinear problem, and the second-order CGT only considers stretching due to the linear dynamics. While previous studies found that a particularly sensitive direction in the second-order CGT indicated that the higher-order terms along this direction are significantly larger than the other terms [4], this is not true for aerocapture. To find a dynamics-informed direction that considers nonlinearities, the tensor eigenpairs of the HOCGTs can be evaluated, and these directions can be used to directionalize the DSTTs [17, 23].

To find the direction of initial perturbation that results in the largest magnitude final state perturbation, the squared  $L^2$  norm of  $\mathbf{x}$  at a later time with respect to the state at a prior time can be evaluated [23]. When using a linear propagation of the state, this expression leads to the definition of the second-order CGT:

$$\|\Phi_{(t_z, t_y)} \mathbf{x}_y\|^2 = \mathbf{x}_y^\top \Phi_{(t_z, t_y)}^\top \Phi_{(t_z, t_y)} \mathbf{x}_y = \mathbf{x}_y^\top \mathbf{C}_{(t_z, t_y)}^{[2]} \mathbf{x}_y. \quad (27)$$

When considering higher-order terms of the Taylor series expansion in the solution for  $\mathbf{x}_z$ , the squared norm of the state at  $t_z$  with respect to the state at  $t_y$  is:

$$\mathbf{x}_z^\top \mathbf{x}_z = \mathbf{C}^{[2]} \mathbf{x}_y^2 + \tilde{\Phi}^{[3]} \mathbf{x}_y^3 + \tilde{\Phi}^{[4]} \mathbf{x}_y^4 + \dots, \quad (28)$$

and the higher-order tensor maps for third- and fourth-order are given by:

$$\tilde{\Phi}^{[3], \kappa_1 \kappa_2 \kappa_3} = \phi^{i, \kappa_1} \phi^{i, \kappa_2 \kappa_3}, \quad \text{and} \quad (29)$$

$$\tilde{\Phi}^{[4], \kappa_1 \kappa_2 \kappa_3 \kappa_4} = \frac{1}{3} \phi^{i, \kappa_1} \phi^{i, \kappa_2 \kappa_3 \kappa_4} + \frac{1}{4} \phi^{i, \kappa_1 \kappa_2} \phi^{i, \kappa_3 \kappa_4}. \quad (30)$$

Jenson and Scheeres showed that a perturbation in the direction of the eigenvector corresponding to the maximum eigenvalue of the HOCGTs will cause the maximum  $L^2$  norm magnitude perturbation in the final state [23]. Thus, while the second-order CGT eigenpair can be used to determine the direction of maximum stretching due to the *linear* dynamics, the HOCGT eigenpairs can be used to determine the direction of maximum stretching due to the *higher-order* dynamics. The higher-order tensor z-eigenpair problem is similar to the matrix eigenpair problem,  $\mathbf{Av} = \lambda \mathbf{v}$ , but extended to higher orders,  $\mathcal{T}^{(m)} \mathbf{v}^{m-1} = \lambda \mathbf{v}$  for  $\mathbf{v}^\top \mathbf{v} = 1$ . These eigenpairs are found using the Shifted-Symmetric Higher-Order Power Method (SS-HOPM) algorithm [24].

A few considerations were taken when utilizing SS-HOPM. As SS-HOPM requires symmetric tensors, we compute symmetric tensors  $\mathbf{C}^{[m]}$  such that  $\tilde{\Phi}^{[m]} = \mathbf{C}^{[m]} \mathbf{x}^m$  [23]. The MATLAB Tensor Toolbox is used to perform this operation [25]. Then, these  $\mathbf{C}^{[m]}$  for  $m > 2$  are the HOCGTs. Additionally, SS-HOPM does not guarantee convergence to the maximum eigenvalue, merely an eigenvalue, so 100 initial guesses are sampled from the unit ball and evaluated with SS-HOPM to find candidates  $\mathbf{v}_i$ . The vectors are de-duplicated by removing all vectors which have a dot product with another  $\mathbf{v}_i$  greater than  $\cos(10^{-3} \text{ rad})$ . The eigenvector corresponding to the largest eigenvalue of the remaining vectors is selected as the maximal direction. While this method does not guarantee convergence to the largest eigenvalue, especially when the eigenvalues are close in magnitude, it does improve convergence over using a single initial guess.

### C. Augmented Higher-Order Cauchy Green Tensors

The HOCGTs described above find the direction that maximizes the final perturbation magnitude for the entire states. However, for certain guidance and navigation applications, we are interested in looking at the direction of sensitivity for key nonlinear states. In the following sections, we propose two augmented HOCGT formulations. First, we introduce selective HOCGTs (sCGTs), which can be used to find the direction that leads to the largest magnitude change for specific states which are known to be nonlinear. Second, we introduce quantity-of-interest HOCGTs (qCGTs), which find the direction that leads to the largest magnitude change for a quantity of interest that is a function of the state.

#### 1. Selective Higher-Order Cauchy Green Tensors

While the HOCGTs can accurately identify nonlinearity for the full state [23], certain states are of more interest for performance analysis than others. To understand dynamic sensitivity in these key states, we are most interested in obtaining the directions that correspond to the maximum magnitude change in those states,  $\xi = \mathbf{Sx} \in \mathbb{R}^w$ , instead of the entire state vector,  $\mathbf{x}$ .  $\mathbf{S} \in \mathbb{R}^{w \times n}$  is a constant selection matrix where  $w \leq n$ , where each row is a Cartesian basis vector along the state selected, and the selected states  $\xi$  are in  $\mathbb{R}^w$ . Here we derive sCGTs, whose tensor eigenpairs can be used to find the maximum stretching direction for the selected states.

The expression to propagate the selected states  $\xi$  from  $t_y$  to  $t_z$  can be written using STTs as:

$$\xi_z^i = \sum_{p=1}^m \frac{1}{p!} S^{i,j} \phi_{(t_z, t_y)}^{j, \kappa_1 \dots \kappa_p} x_y^{\kappa_1} \dots x_y^{\kappa_p}, \quad (31)$$

and the analog to HOCGT Eq. (28) in for sCGTs is:

$$\xi_z^\top \xi_z = \mathcal{S}^{[2]} \mathbf{x}_y^2 + \tilde{\mathcal{S}}^{[3]} \mathbf{x}_y^3 + \tilde{\mathcal{S}}^{[4]} \mathbf{x}_y^4 + \dots, \quad (32)$$

where  $\mathcal{S}^{[2]}$  is the second-order sCGT, which is already symmetric by definition. The third- and fourth-order  $\tilde{\mathcal{S}}^{[m]}$  coefficients are not supersymmetric in general. The coefficients are defined as:

$$\mathcal{S}^{[2], \kappa_1 \kappa_2} = S^{i,j} \phi^{j, \kappa_1} S^{i,k} \phi^{k, \kappa_2}, \quad (33)$$

$$\tilde{\mathcal{S}}^{[3], \kappa_1 \kappa_2 \kappa_3} = S^{i,j} \phi^{j, \kappa_1} S^{i,j} \phi^{j, \kappa_2 \kappa_3}, \quad \text{and} \quad (34)$$

$$\tilde{\mathcal{S}}^{[4], \kappa_1 \kappa_2 \kappa_3 \kappa_4} = \frac{1}{3} S^{i,j} \phi^{j, \kappa_1} S^{i,j} \phi^{j, \kappa_2 \kappa_3 \kappa_4} + \frac{1}{4} S^{i,j} \phi^{j, \kappa_1 \kappa_2} S^{i,j} \phi^{j, \kappa_3 \kappa_4}. \quad (35)$$

These again must be symmetrized in order to solve the eigenproblem using SS-HOPM such that  $\tilde{\mathcal{S}}^{[m]} = \mathcal{S}^{[m]} \mathbf{x}^m$ . The  $\mathcal{S}^{[m]}$  are the higher-order sCGTs.

## 2. Quantity-of-Interest Higher-Order Cauchy Green Tensors

Similarly, certain stretching directions are more significant to key quantities of interest. For aerocapture, quantities of interest could include specific orbital energy (Eq. (12)) or apoapsis radius (Eq. (10)), both of which are key factors for a successful aerocapture. If we primarily want to predict apoapsis radius precisely, we must identify what directions impact error for this direction most. Given a generic vector-valued quantity of interest function  $\mathbf{q} = \mathbf{q}(\mathbf{x}_z)$ , qCGTs are defined to find the direction which this quantity is most sensitive to. The Taylor series expansion of  $\mathbf{q}$  about the state at previous time  $t_y$ ,  $\mathbf{x}_y$  is:

$$q_z^i \simeq \sum_{p=1}^M \frac{1}{p!} \frac{\partial^p q_z^i}{\partial x_y^{\gamma_1} \dots \partial x_y^{\gamma_p}} x_y^{\gamma_1} \dots x_y^{\gamma_p}. \quad (36)$$

To derive the qCGTs, we are interested in coefficients of the quantity  $\mathbf{q}^T \mathbf{q}$ , namely:

$$\mathbf{q}_z^\top \mathbf{q}_z = \mathbf{Q}^{[2]} \mathbf{x}_y^2 + \tilde{\mathbf{Q}}^{[3]} \mathbf{x}_y^3 + \tilde{\mathbf{Q}}^{[4]} \mathbf{x}_y^4 + \dots \quad (37)$$

Because  $\mathbf{q}$  is a function of the state at  $t_z$ , but the state perturbation is propagated from  $t_y$ , the chain rule is employed to relate the change in the later state to the change in the prior state. The first-order coefficient in the expansion in

Eq. (36) is:

$$\frac{\partial q_z^i}{\partial x_y^{\gamma_1}} = \frac{\partial q_z^i}{\partial x_z^{\gamma_2}} \frac{\partial x_z^{\gamma_2}}{\partial x_y^{\gamma_1}}. \quad (38)$$

By noting that

$$\frac{\partial x_z^{\gamma_2}}{\partial x_y^{\gamma_1}} = \phi_{(t_z, t_y)}^{\gamma_2, \gamma_1}, \quad (39)$$

and defining

$$\eta^{i, \gamma_2} = \frac{\partial q_z^i}{\partial x_z^{\gamma_2}}, \quad (40)$$

$$\eta^{i, \gamma_2 \gamma_3} = \frac{\partial^2 q_z^i}{\partial x_z^{\gamma_2} \partial x_z^{\gamma_3}}, \quad \text{and} \quad (41)$$

$$\eta^{i, \gamma_2 \gamma_3 \gamma_4} = \frac{\partial^3 q_z^i}{\partial x_z^{\gamma_2} \partial x_z^{\gamma_3} \partial x_z^{\gamma_4}}, \quad (42)$$

we can write the higher-order qCGT coefficients as:

$$\tilde{Q}^{[2], \kappa_1 \kappa_2} = D_{[1]}^{i, \kappa_1} D_{[1]}^{i, \kappa_2}, \quad (43)$$

$$\tilde{Q}^{[3], \kappa_1 \kappa_2 \kappa_3} = D_{[1]}^{i, \kappa_1} D_{[2]}^{i, \kappa_2 \kappa_3}, \quad \text{and} \quad (44)$$

$$\tilde{Q}^{[4], \kappa_1 \kappa_2 \kappa_3 \kappa_4} = \frac{1}{3} D_{[1]}^{i, \kappa_1} D_{[3]}^{i, \kappa_2 \kappa_3 \kappa_4} + \frac{1}{4} D_{[2]}^{i, \kappa_1 \kappa_2} D_{[2]}^{i, \kappa_4 \lambda_4}. \quad (45)$$

where  $D_{[i]}$  is the  $i^{\text{th}}$ -order coefficient of the Taylor series expansion in Eq. (36),

$$D_{[1]}^{i, \kappa_1} = \eta^{i, j} \phi^{j, \kappa_1}, \quad (46)$$

$$D_{[2]}^{i, \kappa_1 \kappa_2} = \eta^{i, jl} \phi^{l, \kappa_2} \phi^{j, \kappa_1} + \eta^{i, j} \phi^{j, \kappa_1 \kappa_2}, \quad \text{and} \quad (47)$$

$$D_{[3]}^{i, \kappa_1 \kappa_2 \kappa_3} = \eta^{i, jlm} \phi^{m, \kappa_3} \phi^{l, \kappa_2} \phi^{j, \kappa_1} + \eta^{i, jl} \phi^{l, \kappa_2 \kappa_3} \phi^{j, \kappa_1} \\ + \eta^{i, jl} \phi^{l, \kappa_2} \phi^{j, \kappa_1 \kappa_3} + \eta^{i, jl} \phi^{l, \kappa_3} \phi^{j, \kappa_1 \kappa_2} + \eta^{i, j} \phi^{j, \kappa_1 \kappa_2 \kappa_3}, \quad (48)$$

Once the tensors are symmetrized such that  $\tilde{Q}^{[m]} = Q^{[m]} \mathbf{x}^m$ , the  $Q^{[m]}$  are the higher-order qCGTs.

#### D. Comparison of Higher-Order Cauchy Green Tensor Eigenpairs

We now compare the tensor eigenpairs of the novel augmented HOCGTs with the original HOCGT eigenpairs to demonstrate that (1) the eigenpairs vary for each HOCGT type and order, (2) the maximal mode in the higher-order dynamics changes throughout the trajectory, while the linear dynamics do not exhibit this modal variation, and (3) a perturbation in the direction of the eigenvector of the maximum eigenvalue of an augmented HOCGT results in the largest magnitude change in its objective. Fig. 4 compares the tensor eigenpairs corresponding to the maximum eigenvalue

for the second- through fourth-order HOCGTs and augmented HOCGTs for  $(t_{k+1}, t_k)$ . The second-order eigenpairs are found using MATLAB's `eig` function and the higher-order eigenpairs are found using the SS-HOPM algorithm from the Tensor Toolbox [26]. The HOCGTs (see Section IV.B) are compared with the sCGTs for position, velocity, and flight path angle (see Section IV.C.1), and qCGTs for specific energy using quantity of interest function Eq. (12) (see Section IV.C.2). When comparing orders, we can clearly see that the second-order stretching direction, which corresponds to linear dynamics, does not align with the higher-order directions for any HOCGT method. Therefore, using the second-order CGT direction is not appropriate for directionalizing second- and third-order DSTTs for aerocapture because it does not capture the direction of maximum stretching in the higher-order dynamics. Additionally, the sCGTs and  $\varepsilon$ -qCGTs do not have the same dominant eigenvector as the original HOCGTs. If the performance analysis goal is to track these key quantities, using the HOCGT directions for DSTT directionalization could lose higher-order information related to the coordinates important to the quantity of interest while keeping other less important directions.

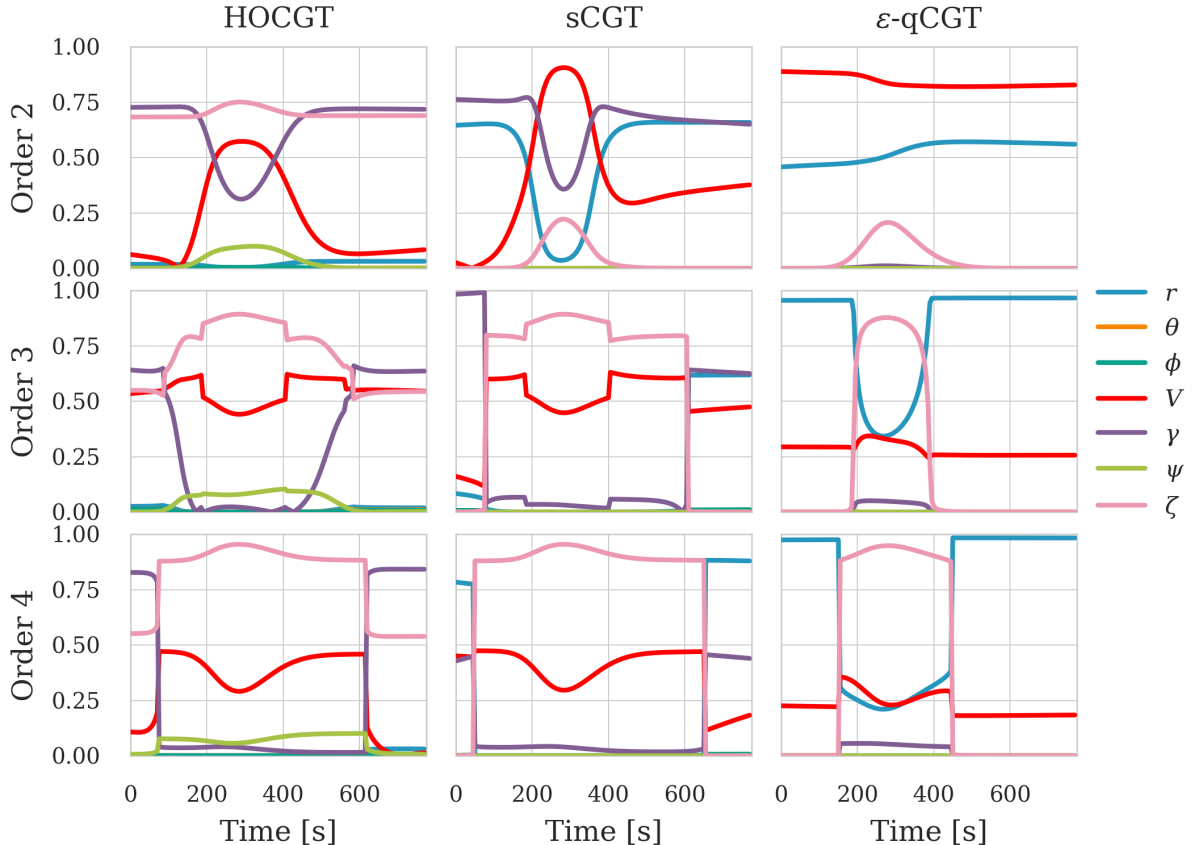


**Fig. 4** Eigenvectors of the maximum eigenvalue for different HOCGT constructions from  $(t_{k+1}, t_k)$ . The sCGTs select position, velocity, and flight path angle; the  $\varepsilon$ -qCGTs are in terms of energy.

Fig. 4 also demonstrates that the dominant mode of the higher-order dynamics switches throughout flight. The maximum eigenvalue of the third-order HOCGTs and sCGTs changes at approximately 200 and 400 seconds, which

causes the noticeable discontinuity in the eigenvector direction for  $V$  and  $\ln(\rho)$ . The two largest eigenvalues, denoted as  $\lambda_1$  and  $\lambda_2$ , found from SS-HOPM for the third-order HOCGTs or augmented HOCGTs are shown in Fig. 5. The ordering of which eigenvalue is dominant is seen to switch through time between  $\lambda_1$  and  $\lambda_2$ . This indicates that the dominant mode of the nonlinear dynamics switches during maximum dynamic pressure, where the aerodynamic accelerations exceed the gravitational accelerations (as shown in Fig. 1), as gravitational accelerations become less significant and atmospheric accelerations dominate the dynamics.

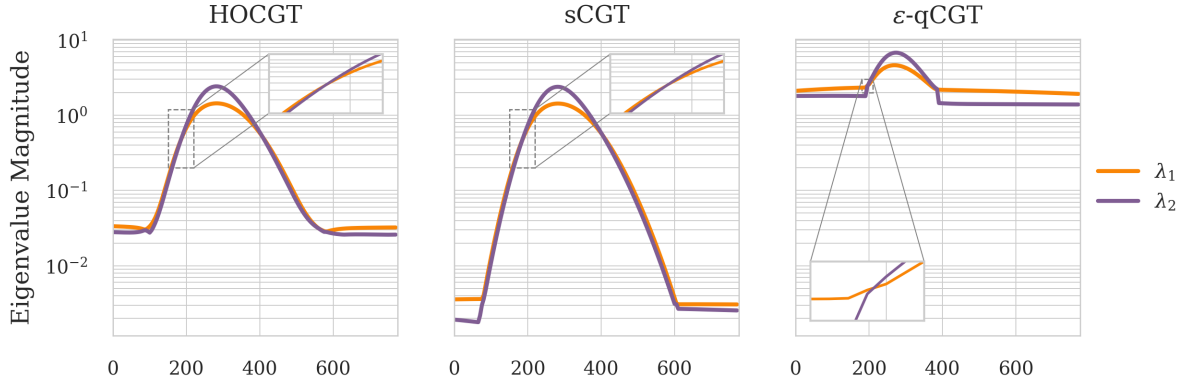


**Fig. 5** Top two eigenvalues of the third-order HOCGTs found from SS-HOPM for  $(t_{k+1}, t_k)$

In addition to comparing the directions for different HOCGT constructions, we also verify that each HOCGT correctly identifies the direction that produces the largest final perturbation in the relevant objective (the total state norm for HOCGTs, selected states norm for sCGTs, and apoapsis radius for the  $r_a$ -qCGTs). To evaluate this, perturbations are propagated along seven orthogonal directions: the maximal third-order HOCGT or augmented HOCGT direction and six orthogonal directions (which span the state space). The perturbations are mapped through the dynamics over  $(t_f, t_0)$  using numerical integration. Fig. 6 shows the relative final objective magnitudes for each direction set. We express each objective as a relative magnitude, normalized by the magnitude obtained from the maximal stretching direction, so we can interpret the result as a fraction for comparison. For the HOCGT maximal stretching direction in Fig. 6a, the objective is the norm of difference between the perturbed final state and the nominal final state for all seven directions, normalized by this quantity for the perturbation along the maximal stretching direction:

$$\frac{\|\mathbf{x}_f^{\text{pert}} - \mathbf{x}_f^{\text{nom}}\|}{\|\mathbf{x}_f^{\text{pert}} - \mathbf{x}_f^{\text{nom}}\|_{0^\circ}} \quad (49)$$

Likewise, the norm of the difference in the final perturbed selected states and the final nominal selected states normalized by this quantity for the perturbation along the maximal stretching direction is shown in Fig. 6b:

$$\frac{\|\boldsymbol{\xi}_f^{\text{pert}} - \boldsymbol{\xi}_f^{\text{nom}}\|}{\|\boldsymbol{\xi}_f^{\text{pert}} - \boldsymbol{\xi}_f^{\text{nom}}\|_{0^\circ}}, \quad (50)$$

and the absolute value of the difference between the final perturbed apoapsis radius and the nominal apoapsis radius normalized by this quantity for the perturbation along the maximal stretching direction are shown in Fig. 6c:

$$\frac{|r_a^{\text{pert}} - r_a^{\text{nom}}|}{|r_a^{\text{pert}} - r_a^{\text{nom}}|_{0^\circ}}. \quad (51)$$

For all HOCGTs, the perturbation along the eigenvector for the maximum eigenvalue from  $(t_f, t_0)$  from the third-order HOCGT or augmented HOCGT induces the largest magnitude change in that coordinate. This indicates that the SS-HOPM solver does identify a direction of sensitivity for the nonlinear dynamics. Note that the y-axis is log scale, and there is still an order of magnitude difference in Fig. 6a and Fig. 6b between the second-largest and largest relative objective change. For cases where the largest and second-largest relative objective changes are close, it may be prudent to keep more than one direction during DSTT construction (i.e.  $l > 1$ ), depending on desired accuracy.

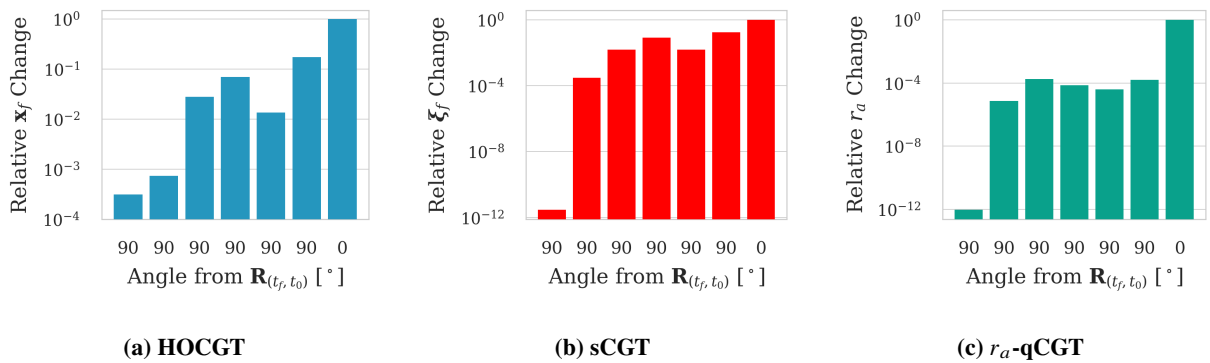


**Fig. 6 Final state and quantity of interest change for orthogonal initial perturbation directions.**

These results also show that the direction of maximum stretching is both clearly time-varying throughout the trajectory and variable between expansion orders, so a time-varying higher-order  $\mathbf{R}_{[p]}$  direction could be beneficial for DSTT directionalization. These results also show that the HOCGTs and augmented HOCGTs correctly identify the direction that leads to the largest magnitude final perturbation in desired objective.

## V. Results

The previous sections presented multiple methods for finding maximum stretching directions using a higher-order Taylor series expansion of the dynamics with the goal of using these directions to construct more accurate DSTTs. In the following sections, we will compare DSTTs constructed using different  $\mathbf{R}_{[p]}$  matrices in terms of the normalized Frobenius norm error between DSTTs and the STTs, perturbation propagation accuracy as a function of alignment with the  $\mathbf{R}_{[p]}$  direction, and prediction accuracy for quantities of interest. All DSTT state perturbations are propagated using Eq. (19), and all STT state perturbations are propagated using Eq. (15).

The following Taylor series approximations were compared:

- 1)  $\Phi$ , the STM;
- 2)  $\phi^{[2]}$ , the second-order STT;
- 3) 1-DSTT, the third-order DSTTs computed with the maximal eigendirection from the second-order CGT for both higher orders such that  $\mathbf{R}_{[2]} = \mathbf{R}_{[3]} \in \mathbb{R}^{1 \times 7}$  and  $\mathbf{y} \in \mathbb{R}$ ;
- 4) 3-DSTT, the third-order DSTTs computed using the eigenvectors corresponding to the largest three eigenvalues of the second-order CGT for both higher orders such that  $\mathbf{R}_{[2]} = \mathbf{R}_{[3]} \in \mathbb{R}^{3 \times 7}$  and  $\mathbf{y} \in \mathbb{R}^3$ ;
- 5) 6-DSTT, the third-order DSTTs computed using the eigenvectors corresponding to the largest six eigenvalues of the second-order CGT for both higher orders such that  $\mathbf{R}_{[2]} = \mathbf{R}_{[3]} \in \mathbb{R}^{6 \times 7}$  and  $\mathbf{y} \in \mathbb{R}^6$ ;
- 6) hoDSTT, the third-order DSTTs using the maximal eigenvector of the third- and fourth-order HOCGTs to directionalize the second- and third-order DSTTs respectively such that  $\mathbf{R}_{[2]} \neq \mathbf{R}_{[3]}$ ;
- 7) sDSTT, the third-order DSTTs using the maximal eigenvector of the third- and fourth-order sCGTs (selecting position, velocity, and flight path angle) to directionalize the second- and third-order DSTTs respectively such that  $\mathbf{R}_{[2]} \neq \mathbf{R}_{[3]}$ ;
- 8)  $\varepsilon$ -qDSTTs, the third-order DSTT using the maximal eigenvector of the third- and fourth-order qCGTs (with energy as the quantity of interest function) to directionalize the second- and third-order DSTTs respectively such that  $\mathbf{R}_{[2]} \neq \mathbf{R}_{[3]}$ ;
- 9) and  $r_a$ -qDSTTs, the third-order DSTT using the maximal eigenvector of the third- and fourth-order qCGTs (with apoapsis radius as the quantity of interest function) to directionalize the second- and third-order DSTTs respectively such that  $\mathbf{R}_{[2]} \neq \mathbf{R}_{[3]}$ .

## A. DSTT Approximation Accuracy

To evaluate the accuracy of each DSTT construction, the normalized Frobenius norm error between DSTTs and STTs and perturbation propagation accuracy for different perturbation directions are computed.

### 1. Normalized Frobenius Norm Error

To determine how well a given DSTT approximates the original STT, the normalized Frobenius norm error is computed as:

$$\epsilon_{\mathcal{F}} = \frac{\left\| \phi^{i, \gamma_1 \dots \gamma_p} - \psi^i R_{[p]}^{\gamma_1} \dots R_{[p]}^{\gamma_p} \right\|_{\mathcal{F}}}{\left\| \phi^{i, \gamma_1 \dots \gamma_p} \right\|_{\mathcal{F}}}, \quad (52)$$

where time indices are omitted for clarity. The Frobenius norm is the square root of the sum of the squared entries of the tensor. Lower error indicates more similarity between the DSTT and STT. Fig. 7 shows the normalized Frobenius norm percent error for various DSTT methods to propagate over the time domain  $(t_{k+1}, t_k)$ . As apoapsis radius is only a function of the final state, the apoapsis radius qDSTT cannot be compared for this time domain. The large initial errors

for some methods indicate that the DSTTs are inaccurate reconstructions of the STTs for approximately the first and last 100 seconds. In this region, the STTs near zero, indicating that there is low nonlinearity. The following discussions will focus on accuracy near maximum dynamic pressure (see Fig. 1) as the dynamics exhibit the most nonlinearity in this region.

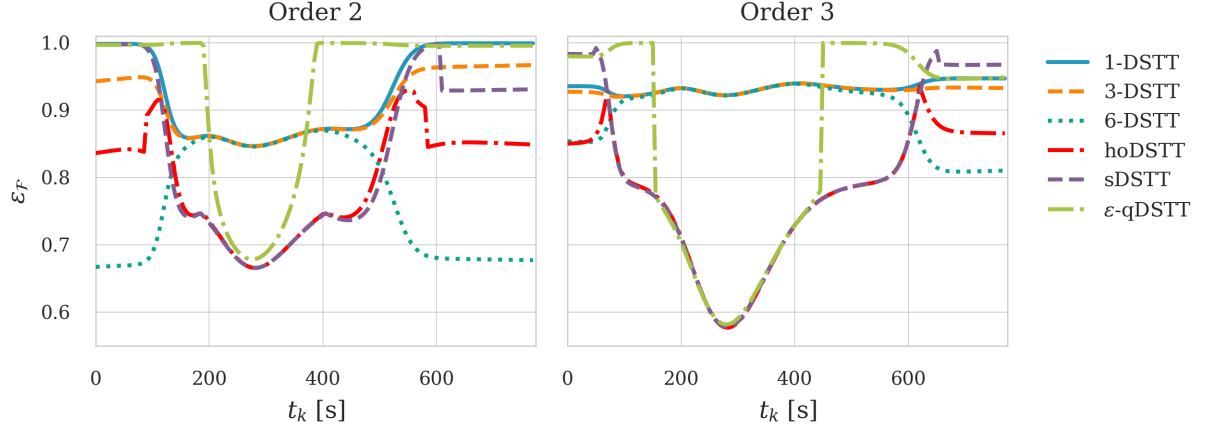


**Fig. 7** Normalized Frobenius norm error for different DSTT approximations mapping from  $(t_{k+1}, t_k)$ .

When evaluating DSTTs constructed with varying  $\mathbf{y}$  dimensions (the 1-DSTT, 3-DSTT, and 6-DSTT), the initial error (between 0 and approximately 100 seconds) is improved when increasing the dimension of  $\mathbf{y}$ . However, the 1-DSTT, 3-DSTT, and 6-DSTT are equivalent from approximately 200 to 400 seconds, which corresponds to peak dynamic pressure (see Fig. 1). Accuracy is critical during this region, where small error in DSTT perturbation propagation during this region could compound and greatly impact terminal perturbation propagation accuracy. While the 6-DSTT is the most accurate of these DSTTs, there is little benefit to using a DSTT with this large of a latent dimension over the regular STT. Tensor contraction operations are still required to propagate a perturbation, rather than only matrix-vector multiplication for DSTTs with a single latent dimension (see Eq. (19)). In Fig. 8, the eigenvalues over  $(t_{k+1}, t_k)$  for the second-order CGT clearly show that  $\lambda_1$  is between 10% and 30% greater than the other eigenvalues for all times. This indicates that a single dimension for  $\mathbf{y}$  is sufficient to capture the dominant linear effects of the dynamics, and adding additional latent dimensions in the original DSTT formulation provides only marginal improvement in approximation accuracy.

However, Fig. 7 shows marked improvement when using the DSTTs constructed with the HOCGT, sCGT, and qCGT directions. The hoDSTT's error is lower than the original DSTTs (1-DSTT, 3-DSTT, and 6-DSTT) for the entire trajectory. This demonstrates that for problems where the second-order and higher-order maximum stretching directions are not well aligned, there is a benefit to using the higher-order directions to construct the DSTTs. When constructing a second-order DSTT, using the maximum stretching direction of the third-order HOCGT, rather than the maximum

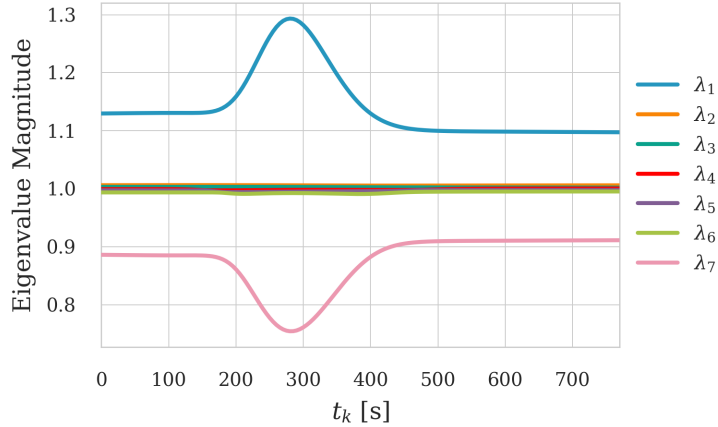


**Fig. 8 Eigenvalue magnitudes for  $(t_{k+1}, t_k)$  for second-order CGT.**

stretching direction for the linear dynamics (second-order CGT maximal eigenvector), results in a DSTT which preserves more of the original STT.

The sDSTT and  $\varepsilon$ -qDSTT have inferior error to the hoDSTT, especially for the initial and final times. While this indicates some accuracy loss during the initial and final time periods, these DSTTs preserve the high accuracy during the critical maximum dynamic pressure region and outperform the original DSTTs in that region. Because maximum dynamic pressure has a great impact on  $\xi$  and  $\varepsilon$ , it is more important for sDSTTs and  $\varepsilon$ -qDSTTs to retain accuracy during this period.

In conclusion, using a higher-order direction with a single latent dimension improves DSTT approximation accuracy in the Frobenius norm sense over using a larger latent dimension with more lower-order directions.

## 2. DSTT Perturbation Propagation Accuracy

In this section, we will explore the propagated perturbation accuracy for varying initial perturbation directions on the unit sphere for second-order scalar latent dimension hoDSTTs. The scalar latent variable magnitude  $|y| = |R_{[2]}^i \delta x_0^i|$  is maximized when  $\mathbf{R}_{[2]}$  is parallel to  $\delta \mathbf{x}_0$ . Therefore, the DSTTs are more accurate for perturbations in directions near  $\mathbf{R}$  such that  $y$  is greater in magnitude, as can be seen from Eq. (19). This is the motivation for why the maximal linear stretching direction was originally chosen as the DSTT directionalization direction: it preserves the STT terms in a direction known to be nonlinear, where the STM will perform poorly.

To demonstrate the efficacy of using HOCGTs (and by proxy sCGTs and qCGTs) to directionalize DSTTs, the following study was conducted. Given the maximal eigenvector of the third-order HOCGT over the entire timespan  $(t_f, t_0)$ ,  $\mathbf{R}_{[2]}$ , and a vector orthogonal to it,  $\mathbf{u}$ , such that  $\mathbf{R}_{[2]} \cdot \mathbf{u} = 0$ , we find vectors in directions  $\delta \mathbf{x}_0 \propto \cos(\kappa) \mathbf{R}_{[2]} + \sin(\kappa) \mathbf{u}$  for  $\kappa \in [0, 90]$  degrees. Low  $\kappa$  angles correspond to directions near  $\mathbf{R}_{[2]}$ . Fig. 9 shows the norm of Taylor series perturbation propagation error from the integrated solution for 25 angles  $\kappa \in [0, 90]$  degrees, where each initial

perturbation direction is scaled to have a nondimensional initial magnitude of  $10^{-6}$ .

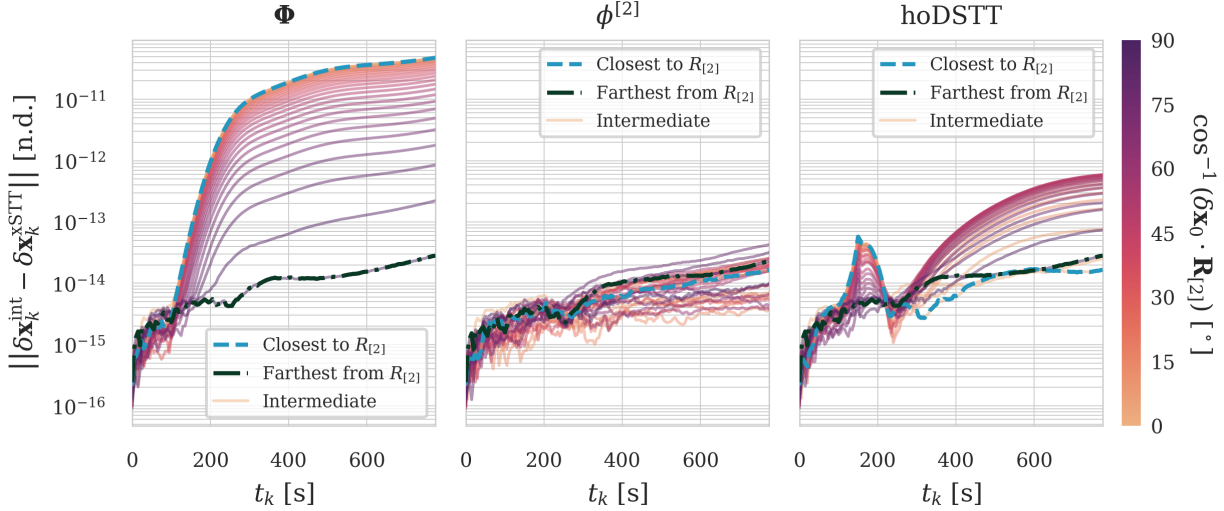


**Fig. 9 Perturbation propagation accuracy per perturbation magnitude along the  $R$  direction**

The STM performs worse for directions near  $\mathbf{R}_{[2]}$ , but is more accurate for perturbations orthogonal to  $\mathbf{R}_{[2]}$ . This is consistent with the fact that a perturbation along the  $\mathbf{R}_{[2]}$  direction should lead to the maximum final magnitude state perturbation (for linear and second-order dynamics). The second-order STT errors are near machine precision throughout the trajectory for all directions. When using a second-order hoDSTT directionalized along the third-order HOCGT maximal eigenvector ( $\mathbf{R}_{[2]}$ ), the error is still generally low for directions far from  $\mathbf{R}_{[2]}$ . Interestingly, it is also low for directions close to  $\mathbf{R}_{[2]}$ . The directions between 30 and 60 degrees from  $\mathbf{R}_{[2]}$  have the largest error for the hoDSTT method, but the error for these perturbations is still lower than the error for the same perturbations propagated with only the STM.

Because the magnitude of  $y$ ,  $|y| = |R_{[2]}^i \delta x_0^i|$ , is maximized for  $\delta x_0$  directions near parallel  $\mathbf{R}_{[2]}$ , even a single latent dimension hoDSTT improves perturbation propagation accuracy for these nonlinear directions. The quantity  $|y|$  is minimized (near zero) for  $\delta x_0$  directions near orthogonal to  $\mathbf{R}_{[2]}$ , but because these directions do not excite nonlinearity in the dynamics, they do not degrade the accuracy of the DSTT.

## B. Quantity of Interest Propagation

To compare DSTT perturbation propagation performance for key quantities of interest, 10,000  $\delta x_0$  samples were taken from the Gaussian distribution in Table 2 and propagated through each Taylor series approximation. The initial zero-mean Gaussian distribution is chosen to be  $1e-14$  in each coordinate in nondimensional units so that that perturbations remain within the linear regime for the initial portions of flight. While DSTTs can also be used to propagate the moments of a Gaussian distribution [4], these results are not included in this paper because they were

consistent with deterministic perturbation propagation.

**Table 2** Initial Standard Deviations in Dimensional Units.

$\sigma_r$ [m]	$\sigma_\theta$ [°]	$\sigma_\phi$ [°]	$\sigma_v$ [m/s]	$\sigma_\gamma$ [°]	$\sigma_\psi$ [°]	$\sigma_\zeta$ [ $\ln(\text{kg}/\text{m}^3)$ ]
2.56	$5.73 \times 10^{-6}$	$5.73 \times 10^{-6}$	$1.52 \times 10^{-3}$	$5.73 \times 10^{-6}$	$5.73 \times 10^{-6}$	$2 \times 10^{-6}$

### 1. Terminal Apoapsis Radius and Energy Prediction

Each  $\delta\mathbf{x}_0$  was propagated through the Taylor series expansion computed from  $(t_f, t_0)$ . The box plot in Fig. 10 compares the terminal apoapsis radius and energy error statistics between the Taylor series propagated solution and the integrated solution for each  $\delta\mathbf{x}_0$ . The box for each quantity depicts the interquartile range (IQR) or the difference between the upper and lower quartile, the mean is shown as a triangle, the median is a horizontal dark line, the whiskers describe 1.5 times the IQR, and the top five outliers are shown as plus marks. Note that the DSTTs expansions are up to third-order, while the first- and second-order STT results are shown. In theory, the DSTT propagated perturbations could have lower error than the second-order STT because of this, although this is not the case in this example.

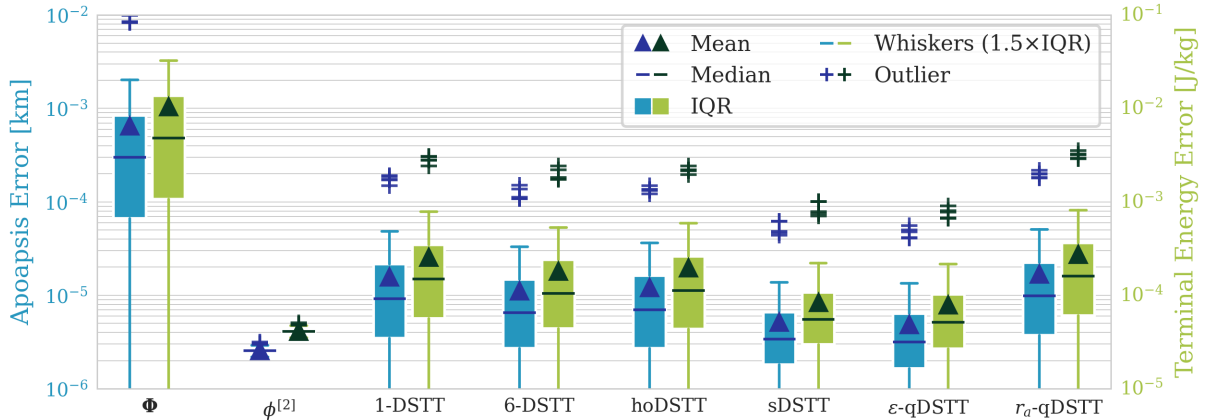


**Fig. 10** Box plot of terminal apoapsis radius and energy error. Only the top five outliers are plotted for clarity.

For terminal energy, the STM has the greatest error values and largest spread in the data, while the second-order STT errors are the lowest magnitude and lowest spread. There is little performance difference for DSTTs with different latent dimensions (the 1-DSTT and 6-DSTT), with only slightly lower median error when increasing the latent dimension from one to six. This again verifies the fact that for systems where the largest eigenvalue magnitude is much greater than the others, there is little improvement to be gained from adding more of the second-order CGT bases to the DSTT. For energy, there is also little difference between the DSTTs constructed with eigenvectors from the second-order CGT (1-DSTT and 6-DSTT) and the DSTT constructed with the dominant eigenpair from the third- and fourth-order CGTs (hoDSTTs). However, when using the maximal eigenpairs of the augmented higher-order sCGT and  $\varepsilon$ -qCGTs to

directionalize the DSTTs, there is an order of magnitude improvement in median energy error and a reduction in error spread. This demonstrates that using an augmented HOCGT parameterized by either the constituent states (in this case,  $r$ ,  $V$ , and  $\gamma$ ) in a quantity of interest function or that function itself leads to improved DSTT propagation performance in that quantity of interest.

However, this finding is not true when looking at the apoapsis radius error. While the same trends as for the energy error hold for the 1-DSTT, 6-DSTT, hoDSTT, sDSTT, and  $\varepsilon$ -qDSTT, the  $r_a$ -qDSTT is less accurate than even the 1-DSTT at predicting terminal apoapsis. While the  $\varepsilon$ -qDSTT was more accurate at predicting energy than DSTTs constructed using other methods, the  $r_a$ -qDSTT is not more accurate at predicting apoapsis radius. This is likely because apoapsis radius is a poorly-conditioned function for quantifying aerocapture performance. Because of the discontinuity in semi-major axis when the trajectory transitions from hyperbolic to elliptical, apoapsis radius exhibits asymptotic behavior mid-flight (see Eq. (10)). This discontinuity is not present for energy, which monotonically decreases throughout an aerocapture trajectory (see Eq. (12)). When computing the apoapsis radius partials to obtain the qCGTs, the discontinuity induces numerical issues, which can in turn result in inaccurate DSTTs. However, the sDSTT that selects the states used in the apoapsis radius function Eq. (10),  $\xi = [r, V, \gamma]^\top$ , is more accurate in apoapsis radius error than the other DSTTs. For applications requiring apoapsis radius prediction, the sDSTT approach (constructing a sCGT for the states in the quantity of interest function) is more accurate than the qDSTT approach (constructing a qCGT using the quantity of interest function).

DSTTs constructed using nonlinear stretching directions for subsets of the state and numerically-stable functions of the state are more accurate at propagating quantities of interest than DSTTs constructed from the second-order CGT maximal eigenpair. However, if the quantity of interest function is discontinuous or has poorly-defined partials, as with apoapsis radius, the DSTTs are not necessarily more accurate. In these cases, constructing an sDSTT with the constituent state variables in the nonlinear quantity of interest function results in improved performance.

## 2. Energy Time History Propagation

The same 10,000  $\delta\mathbf{x}_0$  samples are propagated through Taylor series methods from  $(t_k, t_0)$  and the energy computed for the true integrated perturbed trajectory is compared with the energy computed with the Taylor series approximation. Fig. 11 shows there is agreement between all methods for approximately the first 100 seconds of flight, while all perturbation magnitudes are within the linear convergence region. While the 1-DSTT and 6-DSTT are the best DSTT from approximately 100 to 150 seconds, they grow in error after approximately 200 seconds. For the remainder of the trajectory, the sDSTT,  $\varepsilon$ -qDSTT, and hoDSTT errors are the lowest. However, the hoDSTT accuracy degrades after about 550 seconds. This could be because the HOCGT is not designed to maximize propagation accuracy for the specific energy, but rather preserve the most accuracy for the entire state, so its performance in energy degrades at the expense of preserving accuracy in the total state.

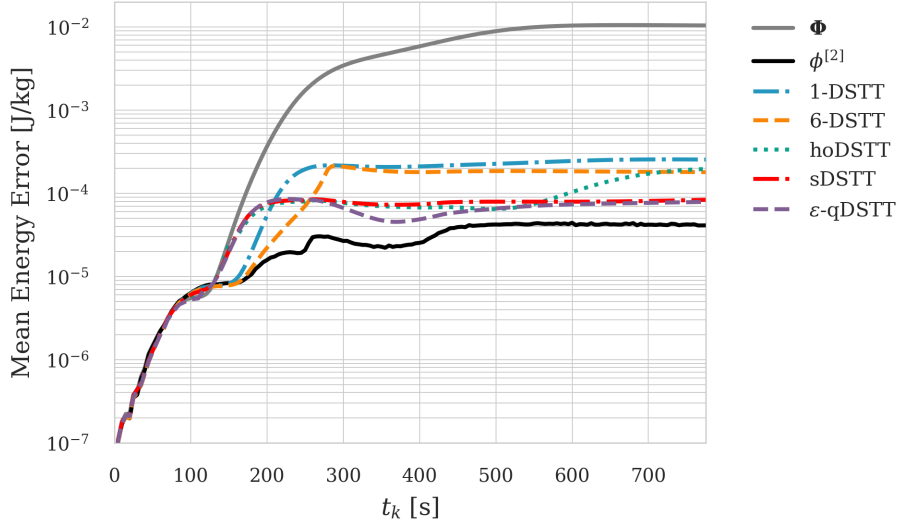


**Fig. 11 Mean energy error from 10,000-case Monte Carlo simulation.**

The  $\varepsilon$ -qDSTT and sDSTT have similarly low energy error throughout time. The  $\varepsilon$ -qDSTT is specifically directionalized along the maximum stretching direction for energy change on each  $(t_k, t_0)$  interval, while the sDSTT is constructed along the direction that maximizes the nondimensional magnitude of vector  $\xi = [r, V, \gamma]^\top$ , some of the the constituent states in energy expression (see Eq. (12)). This shows that the using a sCGT of the constituent states in a quantity of interest function or qCGT for that quantity of interest function can provide similar results.

Although the  $\varepsilon$ -qDSTT has a large normalized Frobenius norm error for the beginning and end of the trajectory (see Fig. 7), there is some improvement in mean energy error propagation for the  $\varepsilon$ -qDSTT over the sDSTT. This demonstrates that while the normalized Frobenius norm error metric quantifies how well a specific DSTT approximation preserves the original STT, it does not take into account the performance for a specific quantity of interest.

## VI. Conclusions

This paper derived new methods for constructing reduced-dimension DSTTs for aerocapture and demonstrated that STTs and DSTTs are effective tools for the highly nonlinear, nonconservative aerocapture dynamical system. Previous work relied on finding the direction of maximum linear stretching to reduce the dimension of the higher-order STTs; in this work, the tensor eigenpairs of HOCGTs and novel augmented HOCGTs were used to construct reduced-dimension DSTTs. The tensor eigenvector of the maximum eigenvalue of a HOCGT is the direction which leads to the maximum final state magnitude perturbation due to the nonlinear dynamics. This idea was extended to develop sCGTs, whose maximal eigenpair determines the direction which leads to the maximum final magnitude perturbation in the nonlinear dynamics for a selected subset of the full state, and qCGTs, whose maximal eigenpair determines the direction which leads to the maximum final magnitude perturbation through the nonlinear dynamics for a nonlinear function of the state.

The latter two augmented HOCGT formulations recognize that certain states matter more than others for aerocapture applications, which can be leveraged to construct a DSTT that is most accurate for a specific application.

DSTTs constructed using these dynamics-informed higher-order directions were shown to have lower Frobenius norm error relative to the STTs. In addition, we showed that a DSTT constructed with these novel directions for a single latent dimension are more accurate for perturbation propagation than DSTTs constructed with the original DSTT linear stretching directions and larger latent dimensions. The novel DSTTs were also more accurate for propagating key quantities of interest than the original DSTTs.

The tensor eigenpairs of augmented HOCGTs can be applied to any nonlinear dynamical system to construct DSTTs while considering nonlinear directions of sensitivity. Other applications for augmented HOCGT tensor eigenpairs include Gaussian mixture model splitting to enable nonlinear, non-Gaussian state distribution propagation.

## Funding Sources

This work was supported by NASA Space Grant Technology Research Fellowship grant number 80NSSC23K1227.

## Acknowledgments

G. Calkins would like to thank Oliver Boodram and Dillon Waxman for their discussions and review of the tensor algebra in this paper, and Jackson Kulik for his insight on tensor eigenpairs.

## References

- [1] Dutta, S., Shellabarger, E., Scoggins, J. B., Gomez-Delrio, A., Lugo, R., Deshmukh, R., Tackett, B., Williams, J., Johnson, B., Matz, D., Geiser, J., Morgan, J., Restrepo, R., and Mages, D., “Uranus Flagship-class Orbiter and Probe Using Aerocapture,” *Proceedings of the AIAA SCITECH 2024 Forum*, AIAA, Orlando, FL, 2024. <https://doi.org/10.2514/6.2024-0714>.
- [2] Park, R. S., and Scheeres, D. J., “Nonlinear Semi-Analytic Methods for Trajectory Estimation,” *Journal of Guidance, Control, and Dynamics*, Vol. 30, No. 6, 2007, pp. 1668–1676. <https://doi.org/10.2514/1.29106>.
- [3] Park, R. S., and Scheeres, D. J., “Nonlinear Mapping of Gaussian Statistics: Theory and Applications to Spacecraft Trajectory Design,” *Journal of Guidance, Control, and Dynamics*, Vol. 29, No. 6, 2006, pp. 1367–1375. <https://doi.org/10.2514/1.20177>.
- [4] Boone, S., and McMahon, J., “Directional State Transition Tensors for Capturing Dominant Nonlinear Effects in Orbital Dynamics,” *Journal of Guidance, Control, and Dynamics*, Vol. 46, No. 3, 2023, pp. 431–442. <https://doi.org/10.2514/1.G006910>.
- [5] Ridderhof, J., Albert, S. W., Tsiotras, P., and Schaub, H., “Linear Covariance Analysis of Entry and Aerocapture Trajectories in an Uncertain Atmosphere,” *Proceedings of the AIAA SCITECH 2022 Forum*, AIAA, San Diego, CA & Virtual, 2022. <https://doi.org/10.2514/6.2022-1216>.
- [6] Joshi, J., Woffinden, D., and Putnam, Z. R., “End-to-End Mars Aerocapture Analysis Using Linear Covariance Techniques

and Robust Trajectory Optimization,” *Proceedings of the 2022 AAS/AIAA Astrodynamics Specialists Conference*, AIAA/AAS, Charlotte, NC, 2022. AAS 22-678.

- [7] Grace, M. J., and McMahon, J. W., “Two-Stage Polynomial Chaos Expansion: An Extension Of Uncertainty Quantification Techniques For Multi-Modal Distributions in Aerocapture,” *Proceedings of the AIAA SCITECH 2022 Forum*, AIAA, San Diego, CA & Virtual, 2022. <https://doi.org/10.2514/6.2022-1769>.
- [8] Albert, S. W., Doostan, A., and Schaub, H., “Finite-Dimensional Density Representation for Aerocapture Uncertainty Quantification,” *Proceedings of the AIAA SCITECH 2021 Forum*, AIAA, Virtual, 2021. <https://doi.org/10.2514/6.2021-0932>.
- [9] Grace, M., and McMahon, J., “Application Of Gaussian Mixture Models For Nonlinear Uncertainty Propagation During Martian Aerocapture,” *Proceedings of the 2020 AAS/AIAA Astrodynamics Specialist Conference*, AAS, Virtual, 2020. AAS 20-485.
- [10] Kulik, J., Ruth, M., Orton-Urbina, C., and Savransky, D., “Applications of Induced Tensor Norms to Guidance Navigation and Control,” *Journal of Guidance, Control, and Dynamics*, Vol. 48, No. 10, 2025, pp. 2180–2198. <https://doi.org/10.2514/1.G009054>.
- [11] Kulik, J., and LeGrand, K. A., “Nonlinearity and Uncertainty Informed Moment-Matching Gaussian Mixture Splitting,” *arXiv preprint*, 2024. <https://doi.org/10.48550/arXiv.2412.00343>.
- [12] Calkins, G. E., Woffinden, D., and McMahon, J., “Efficient Higher-Order Analytical Covariance Analysis For Aerocapture,” *Proceedings of the 2024 AAS/AIAA Astrodynamics Specialists Conference*, AIAA/AAS, Broomfield, CO, 2024. AAS 24-241.
- [13] Calkins, G. E., McMahon, J. W., and Woffinden, D. C., “Dynamics-Informed Higher-Order Uncertainty Quantification for Aerocapture,” *Proceedings of the 2025 AIAA/AAS Spaceflight Mechanics Meeting*, AIAA/AAS, Kaua’i, HI, 2025. AAS 25-317.
- [14] Boodram, O., Boone, S., and McMahon, J., “Efficient Nonlinear Spacecraft Navigation using Directional State Transition Tensors,” *Proceedings of the 2022 AAS/AIAA Astrodynamics Specialists Conference*, AIAA/AAS, Charlotte, NC, 2022. AAS 22-670.
- [15] Zhou, X., Armellin, R., Qiao, D., and Li, X., “Time-Varying Directional State Transition Tensor for Orbit Uncertainty Propagation,” *arXiv preprint*, 2024. <https://doi.org/10.48550/arXiv.2412.07060>.
- [16] Zhou, X., Qiao, D., Malcolm, M., and Li, X., “Efficient Orbit Determination Using Measurement-Directional State Transition Tensor,” *IEEE Transactions on Aerospace and Electronic Systems*, Vol. 61, No. 3, 2025, pp. 8014–8027. <https://doi.org/10.1109/TAES.2025.3527410>.
- [17] Jenson, E. L., and Scheeres, D. J., “Semianalytical Measures of Nonlinearity Based on Tensor Eigenpairs,” *Journal of Guidance, Control, and Dynamics*, Vol. 46, No. 4, 2023, pp. 638–653. <https://doi.org/10.2514/1.G006760>.
- [18] Vihn, N. X., Busemann, A., and Culp, R., *Hypersonic and planetary entry flight mechanics*, The University of Michigan Press, Ann Arbor, MI, 1980.

[19] Lu, P., Cerimele, C. J., Tigges, M. A., and Matz, D. A., “Optimal Aerocapture Guidance,” *Journal of Guidance, Control, and Dynamics*, Vol. 38, No. 4, 2015, pp. 553–565. <https://doi.org/10.2514/1.G000713>.

[20] Deshmukh, R., Dutta, S., Lugo, R., Restrepo, R., Mages, D., Johnson, B., Matz, D., Geiser, J., Scoggins, J. B., Shellabarger, E., Gomez-Delrio, A., and Williams, J., “Performance Analysis of Aerocapture Systems for Uranus Orbiter,” *Proceedings of the AIAA SCITECH 2024 Forum*, AIAA, Orlando, FL, 2024. <https://doi.org/10.2514/6.2024-0716>.

[21] Justh, H. L., Cianciolo, A. D., Hoffman, J., and Allen, G. A., Jr., “Uranus Global Reference Atmospheric Model (Uranus-GRAM): User Guide,” NASA TM-2010017250, Jun. 2021.

[22] Lu, P., “Entry Guidance: A Unified Method,” *Journal of Guidance, Control, and Dynamics*, Vol. 37, No. 3, 2014, pp. 713–728.

[23] Jenson, E. L., and Scheeres, D. J., “Bounding nonlinear stretching about spacecraft trajectories using tensor eigenpairs,” *Acta Astronautica*, Vol. 214, 2024, pp. 159–166. <https://doi.org/10.1016/j.actaastro.2023.10.013>.

[24] Kolda, T. G., and Mayo, J. R., “Shifted Power Method for Computing Tensor Eigenpairs,” *SIAM Journal on Matrix Analysis and Applications*, Vol. 32, No. 4, 2011, pp. 1095–1124. <https://doi.org/10.1137/100801482>.

[25] Bader, B. W., and Kolda, T. G., “Algorithm 862: MATLAB tensor classes for fast algorithm prototyping,” *ACM Transactions on Mathematical Software*, Vol. 32, No. 4, 2006, pp. 635–653. <https://doi.org/10.1145/1186785.1186794>.

[26] Bader, B. W., and Kolda, T. G., “Tensor Toolbox for MATLAB,” <https://www.tensortoolbox.org>, Oct. 2025. Version 3.7.